

FlexiDreamer: Single Image-to-3D Generation with FlexiCubes

Ruowen Zhao^{1,4}, Zhengyi Wang^{2,4}, Yikai Wang², Zihan Zhou³, and Jun Zhu^{2,4}

¹ University of Chinese Academy of Sciences

² Tsinghua University ³ Xidian University ⁴ ShengShu

<https://flexidreamer.github.io>

Input Images

Generated Meshes



Fig. 1: FlexiDreamer for single image-to-3D generation: FlexiDreamer can reconstruct 3D content with detailed geometry and accurate appearance from a single image. We are able to generate a premium textured mesh in approximately one minute.

Abstract. 3D content generation from text prompts or single images has made remarkable progress in quality and speed recently. One of its dominant paradigms involves generating consistent multi-view images followed by a sparse-view reconstruction. However, due to the challenge of directly deforming the mesh representation to approach the target topology, most methodologies learn an implicit representation (such as NeRF) during the sparse-view reconstruction and acquire the target

mesh by a post-processing extraction. Although the implicit representation can effectively model rich 3D information, its training typically entails a long convergence time. In addition, the post-extraction operation from the implicit field also leads to undesirable visual artifacts. In this paper, we propose FlexiDreamer, a novel single image-to-3d generation framework that reconstructs the target mesh in an end-to-end manner. By leveraging a flexible gradient-based extraction known as FlexiCubes, our method circumvents the defects brought by the post-processing and facilitates a direct acquisition of the target mesh. Furthermore, we incorporate a multi-resolution hash grid encoding scheme that progressively activates the encoding levels into the implicit field in FlexiCubes to help capture geometric details for per-step optimization. Notably, FlexiDreamer recovers a dense 3D structure from a single-view image in approximately 1 minute on a single NVIDIA A100 GPU, outperforming previous methodologies by a large margin.

Keywords: 3D Generation · Diffusion Models · FlexiCubes

1 Introduction

3D content technologies allow us to create realistic digital representations of objects, environments and characters, enabling immersive experiences in virtual reality, gaming, animation and various other fields. A system that enables an easy generation of 3D content by non-professional users holds significant value. In spite of the widespread applications, creating premium 3D content often remains a challenging task. Deficient in large-scale 3D training data, 3D native generation methods usually grapple with open-vocabulary generation issues. Drawing inspiration from the advancements in text-to-image synthesis observed in recent 2D content generation such as [54], the emergence of 2D lifting methods facilitates the rapid achievement in 3D content generation field. DreamFusion [49] pioneers a 2D prior-based approach for optimizing a 3D representation via score distillation sampling (SDS), setting a new standard for integrating generalizability into 3D generation. Building upon DreamFusion, recent works including [6, 29, 60, 71, 75], have endeavored to further enhance the quality and diversity of generated 3D assets.

In addition to SDS-based methods, another promising paradigm for 2D lifting methodologies is to utilize an appropriate few-shot reconstruction following a multi-view diffusion model. In this pattern, the fine-tuned 2D diffusion models realize a single image-conditioned novel view synthesis, and then a sparse-view reconstruction framework supervised by generated images is trained to obtain the desired polygonal mesh. However, a direct prediction of triangular meshes necessitates the pre-definition of a simple topology, such as a sphere, and then gradually approximates the target topology through vertex manipulation, edge splitting or edge flipping. Such deforming operations are difficult to perform at a fine scale, thereby struggling to synthesize complex shapes. Therefore, a majority of techniques prefer to train an implicit 3D representation such as NeRF

[44], which is more effective for complex geometry learning in the sparse-view reconstruction, and then extract the textured mesh in a post-processing stage. For example, [19,25,33,35,37] adopt a NeRF-based representation (e.g., [3,38,70]) to model the underlying abundant 3D information and extract the target mesh with Marching Cubes [39]. Despite achieving high-fidelity results, NeRF-based methods require extensive training time and substantial resources especially for high-resolution outputs, due to their reliance on ray marching algorithms for rendering. The intensive computation and prolonged generation time impede their deployment in real-world applications on a large scale. Moreover, the post-processing step typically exposes such methods to reconstruction artifacts and yields an abundance of elements, resulting in the extracted mesh of inferior quality with grid aliasing issues.

In this paper, we introduce the FlexiDreamer framework, which overcomes the limitations of current approaches in the aforementioned paradigm and efficiently generates 3D content in an end-to-end manner. Specifically, FlexiDreamer leverages a flexible gradient-based surface extraction method FlexiCubes [57], which provides a new differentiable shape representation to model 3D information in the sparse-view reconstruction. By utilizing FlexiCubes, our method can predict the underlying surface parameterized by a signed distance implicit function and convert it into an explicit mesh for iterative optimization. This hybrid 3D representation not only preserves the inherent capability of signed distance implicit representation to depict arbitrary topology, but allows for a faster rendering in the form of explicit mesh representation, circumventing the slow volumetric rendering procedure in NeRF and diminishing generation time. Moreover, extracting polygonal mesh from implicit function in each optimization step enables an end-to-end acquisition of the target mesh without any post-processing operation after the completion of training. As a result, the final 3D structure reconstructed by FlexiDreamer is free from any shortcomings associated with post-extraction processes.

However, directly integrating FlexiCubes into our framework tends to be non-trivial. We notice that the original learning pattern of signed distance implicit function in FlexiCubes exhibits a limited generalization ability across different perspectives. To address this, we replace the original pattern with a specially designed neural field aimed at enhancing generalization. Inspired by the scalable representation known as Instant-NGP [45], we incorporate a multi-resolution hashgrid encoding scheme that progressively activates the encoding levels into the neural networks. This hierarchical 3D grid structure, coupled with a lightweight MLP, converges much faster and increases the representation power of neural fields, successfully capturing very fine-grained details. Furthermore, a texture neural field with a similar structure with signed distance function field is also integrated into our framework for mesh surface texture learning.

In summary, FlexiDreamer is an end-to-end framework that obtains the target 3D mesh without additional post-processing manipulation due to the utilization of FlexiCubes. The method enables a rapid generation of photorealistic 3D

assets in the form of explicit meshes from single-view images in approximately 1 minute.

2 Related Works

2.1 3D Generation with Diffusion Models

Recently, 2D diffusion models have achieved notable success in text-to-image generation [54]. However, extending it to 3D generation poses a significant challenge. Existing 3D native diffusion models such as [2, 5, 10, 16, 18, 21, 36, 46, 47, 73, 82, 90] can generate consistent 3D assets within seconds, but they struggle to achieve open-vocabulary 3D generation due to the limited availability of extensive 3D training datasets. On the other hand, inspired by the remarkable progress of text-to-image synthesis in 2D diffusion models, DreamFusion [49] first proposes to distill 3D geometry and appearance from 2D diffusion priors via Score Distillation Sampling (SDS). Later methods [6, 8, 13, 26, 29, 40, 42, 52, 55, 62, 67, 69, 74, 75] build on DreamFusion and further enhance the quality of generated outputs. To tackle potential issues such as the Janus problem, [51, 60, 71, 84] strengthen the semantics of different views when generating multi-view images. Recently, LRM [19, 68] proposes a transformer-based reconstruction model to predict NeRF representation from single image in 5 seconds. Following works [25, 72, 80] combine LRM with pose prediction or multi-view diffusion model to perform a rapid and diverse generation. Moreover, some approaches, such as [7, 9, 28, 31, 43, 53, 63, 65, 65, 66, 76, 78, 79, 85–87, 91], choose Gaussian Splatting [22] or Flexicubes [57] as an alternative 3D representation in reconstruction to avoid the costly volumetric rendering in NeRF.

2.2 Sparse-view Reconstruction with Multi-view Generation

The evolution of 2D lifting methods has facilitated the development of consistent multi-view image generation by diffusion models [30, 34, 58, 61, 81, 83]. With multi-view images obtained, the target 3D asset can be recovered quickly by a sparse-view reconstruction. Zero-1-to-3 [34] incorporates camera pose transformations into 2D diffusion models and realizes image-conditioned novel view synthesis. One-2-3-45 [33] trains a reconstruction framework in conjunction with Zero-1-to-3 and SparseNeuS [38], realizing a rapid 3D generation. SyncDreamer [35] uses spatial volume and depth-wise attention in a 2D diffusion model to generate multi-view consistent images. Wonder3D [37] and Zero123++ [58] extend to generate multi-view RGB and normal images with cross-domain attention layers integrated into diffusion models. These high-fidelity generated images can yield 3D reconstruction via NeuS [70] or other NeRF variants [4, 15, 59]. However, since polygonal meshes are the most widely used 3D representation in downstream tasks, an additional post-processing step, commonly achieved by Marching Cubes [39], is adopted to extract target mesh from the implicit field. This step often encounters issues such as visual artifacts, adversely affecting the quality of the final reconstructed mesh.

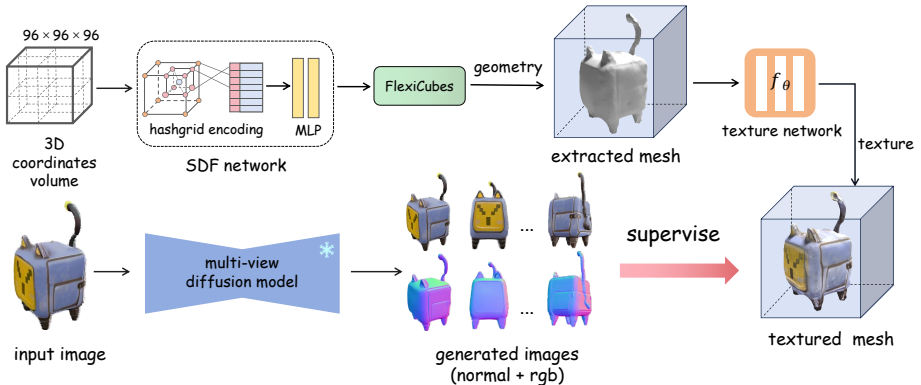


Fig. 2: The pipeline of FlexiDreamer. FlexiDreamer is an end-to-end framework for high-quality 3D generation from a reference image. In each optimization step, we estimate the signed distance field of a bounded space and utilize FlexiCubes to derive an explicit mesh geometry from it. Then texture is applied to the mesh surface by a texture neural network. The entire framework is trained end-to-end on generated images with reconstruction losses.

2.3 Surface Extraction Method

Many previous 3D generation works [25, 33, 35, 37] obtain the final explicit mesh by exporting NeRF representation to mesh-based representation with surface extraction. Marching Cubes (MC) [39] is the most adopted, but it suffers from topological ambiguities and struggles to represent sharp features. Dual Contouring (DC) [20] uses a dual representation where mesh vertices are extracted per cell, and estimates vertex position based on local details.

With the advancement of machine learning, many works explore gradient-based mesh reconstruction schemes, which extract surface from an implicit function encoded via convolutional networks and evaluate objectives on the mesh. DMTet [56] utilizes a differentiable marching tetrahedra layer that converts the implicit signed distance function to explicit mesh, meanwhile maintaining the implicit function’s ability to represent complex topology effectively. However, vertices of extracted mesh in DMTet are unable to move independently, leading to surface artifacts. FlexiCubes [57], which builds on Dual Marching Cube extraction [48], integrates flexibility to the mesh-based representation by introducing extra weight parameters. These gradient-based surface extraction methods not only represent arbitrary typology due to the combination with implicit function, but also provide an end-to-end training scheme.

3 Method

In this section, we present a detailed overview of FlexiDreamer. FlexiDreamer adheres to the generation paradigm that a few-shot reconstruction is combined with

multi-view supervised image generation. Given an input image, a pre-trained diffusion model first generates multi-view RGB and normal images (Sec 3.1). In each iteration of the sparse-view reconstruction, we extract an explicit mesh by FlexiCubes (Sec 3.3) from a signed distance field in the bounded 3D space encoded via a specially-designed network (Sec 3.2). With a texture neural field (Sec 3.4) integrated, rendered RGB images from mesh are obtained by rasterization, which is subsequently used in training objectives (Sec 3.5). The pipeline of our framework is illustrated in Figure 2.

3.1 Multi-view Diffusion Scheme

As depicted in Figure 2, we take advantage of an input RGB image to the pre-trained diffusion model to generate multi-view images. Specifically, we adopt Zero123++ (v1.2) [58], a model trained with both global and local attention incorporated in 2D diffusion to facilitate information exchange across views and modalities. The multi-view RGB images are generated at 6 evenly distributed azimuths and interleaving elevations of -10° and 20° from the diffusion model. Then an RGB image-controlled ControlNet [88] is used to generate corresponding normal images. Compared to other multi-view diffusion models in [26, 32, 34, 35, 60, 71], this capacity of generating normal images in Zero123++ (v1.2) is important in our framework since normal supervisions play a crucial role in enhancing geometry reconstruction.

3.2 Signed Distance Neural Field

We compute an ambient mapping $g : \mathbb{R}^3 \rightarrow \mathbb{R}$, which is parameterized by a signed distance neural field. It is used to define an underlying surface representation when applied to a known input domain (i.e. the 3D coordinates volume space in Figure 2). Due to the bias of neural networks on low-dimensional inputs, we use a positional encoding of the input domain to learn finer surface details. Drawing inspiration from Instant-NGP [45], we incorporate a multi-resolution hash grids positional encoding scheme within the signed distance neural field:

Given an input coordinate $\mathbf{x} \in \mathbb{R}^3$, we map it to the corresponding position at each hash grid resolution and obtain each feature through trilinear interpolation. The encoding features from all resolutions are then concatenated together to form the final encoding of \mathbf{x} . This hierarchical 3D grid structure connected with a lightweight MLP comprises our signed distance neural field, enhancing the representation power of neural fields and realizing a much faster convergence speed.

Despite being encoded in a spatial hierarchy, finer resolutions can not accurately recover surfaces that are misrepresented by coarser ones when activated simultaneously [64]. For this reason, inspired by [27], we only activate an initial set of coarse hash grids, and progressively enable finer hash grids during training to capture more geometric details.

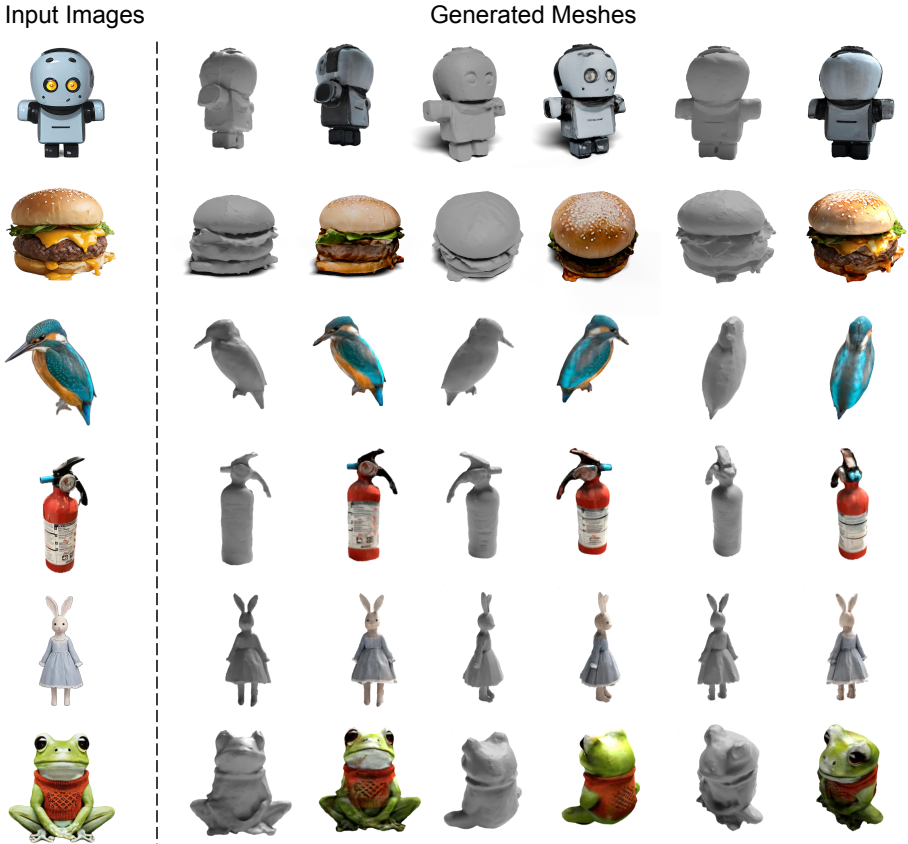


Fig. 3: More examples showcase the 3D assets generated by FlexiDreamer using single-view images. These premium examples highlight the versatility and robustness of FlexiDreamer in handling various object categories and complex geometric structures.

3.3 Mesh Surface Extraction

To directly acquire a polygonal mesh at the end of the sparse view reconstruction, we utilize a flexible gradient-based surface extraction known as FlexiCubes [57] to extract mesh from the implicit signed distance surface at each training iteration. We first locate the positions of zero-crossing u_e in each grid edge of the 3D coordinates volume through linear interpolation according to the underlying mesh surface parameterized by the signed distance field:

$$u_e = \frac{s(x_i) \alpha_i x_j - s(x_j) \alpha_j x_i}{s(x_i) \alpha_i - s(x_j) \alpha_j} \quad (1)$$

$s(x_i)$ and $s(x_j)$, which are with opposite signs, represent the signed distance value of two adjacent grid lattices x_i and x_j respectively. Then the zero-crossing

u_e of each edge in an edge set V_E comprises a typical type of primal face in [48] and each extracted vertex v_d is located by computing the centroid of a face:

$$v_d = \frac{1}{\sum_{u_e \in V_E} \beta_e} \sum_{u_e \in V_E} \beta_e u_e \quad (2)$$

It is noticed that $\alpha \in \mathbb{R}^8$ associated with each grid lattice and $\beta \in \mathbb{R}^{12}$ related to each edge are configured instead of adopting a naive linear interpolation in Equation 1 or centroid definition in Equation 2. These two sets of parameters are introduced to help realize a flexible vertex extraction and capture sharp features on the surface. Both of them are learnable in our training reconstruction framework.

Vertices of the mesh are calculated from a signed distance field by applying Equation 1 and 2 in each cell unit. The extracted mesh is iteratively refined together with the signed distance network using fast differentiable rasterization [24]. The target polygonal mesh can be obtained at the last optimization step without any post-processing procedure.

3.4 Texture Neural Field

A texture neural field is baked onto the iteratively extracted mesh to obtain texture images. Given a camera viewpoint, we rasterize the mesh into an image, which is compared against the ground-truth image. We define the texture neural network:

$$f_\theta(x_i, n_i, \omega_i) \in [0, 1]^3 \quad (3)$$

to generate a 2D image with per-pixel linearly-interpolated surface positions x_i , surface normals n_i and view direction ω_i . Here, both x_i and n_i are obtained from differentiable rasterization. The surface positions x_i are encoded by a multi-resolution hash grid scheme and then fed to the texture network together with normals and view direction to predict per-pixel RGB values in the rendering image. We represent the texture network as a shallow multi-layer perception, with θ as the parameters of the fully-connected layers.

3.5 Training Objectives

FlexiDreamer generates the 3D shape from a single input image and leverages additional side views generated from the multi-view diffusion model to train the reconstruction framework. The overall objective function is defined as:

$$\begin{aligned} \mathcal{L}_{total} = & \mathcal{L}_{rgb} + \mathcal{L}_{mask} + \mathcal{L}_{normal} + \mathcal{R}_{eikonal} \\ & + \mathcal{R}_{laplacian} + \mathcal{R}_{consistency} \end{aligned} \quad (4)$$

where \mathcal{L}_{rgb} , \mathcal{L}_{mask} and \mathcal{L}_{normal} refer to the difference between the rendered images of the extracted mesh and the ground-truths while $\mathcal{R}_{eikonal}$, $\mathcal{R}_{laplacian}$ and $\mathcal{R}_{consistency}$ regularize the mesh to avoid undesired artifacts.

We compute an MSE loss between the rendered image and its corresponding ground truth respectively in \mathcal{L}_{rgb} , \mathcal{L}_{mask} and \mathcal{L}_{normal} . To ensure the learned signed distance values from the neural network are valid, the gradients of signed distance values need to satisfy the eikonal equation [17] (i.e. $\|\nabla f(x_i)\| = 1$). Thus, the eikonal regularization is defined as:

$$\mathcal{R}_{eikonal} = \frac{1}{K} \sum_{i=1}^K (\|\nabla f(x_i)\| - 1)^2 \quad (5)$$

where K refers to the total number of points in the 3D coordinates volume. Moreover, naively locating the extracted vertices unconstrained in each iteration may result in an undesired abrupt surface. Therefore, a penalty term $\mathcal{R}_{laplacian}$ is adopted to avoid a rough mesh surface inspired by [41]. This regularization targets at minimizing each vertex’s distance to the average position of its neighbours. We additionally integrate a normal consistency term $\mathcal{R}_{consistency}$ to further smooth the mesh by minimizing the negative cosine similarity between connected face normals (See Sec 5.3 for details).

4 Implementation Details

In practice, the pretrained multi-view diffusion model in FlexiDreamer is adopted from Zero123++ (v1.2), which is trained on the images blended from Objaverse [11, 12] dataset. The 6 views of RGB and normal outputs from Zero123++ are resized into a resolution of 256×256 to furnish our following end-to-end reconstruction training framework with supervision.

The signed distance neural network consists of a one-layer Multi-Layer Perception with 64 hidden units and a skip connection in the middle. It is also initialized by the geometric initialization present in [1]. The texture neural network has three layers of MLPs with 256 hidden units, where ReLU activations are used for the hidden layer and a sigmoid activation is adopted for the last layer. Furthermore, the grid resolution of 3D coordinates volume is set to 96 to strike a balance between generation speed and quality (see Sec C in Appendix for details).

For the sparse-view reconstruction stage, we train 600 iterations for an optimal generation outcome. The AdamW [23] optimizer is adopted with the learning rate of 1e-3 and 1e-2 for signed distance and texture neural networks respectively.

5 Experiments

5.1 Qualitative Results

To illustrate FlexiDreamer’s scalability on single image-to-3d tasks, we compare its performance with recent state-of-the-art single-view object modeling methods: One-2-3-45 [33], SyncDreamer [35] and Wonder3D [37]. The implementation is based on their open-source code with default parameters.

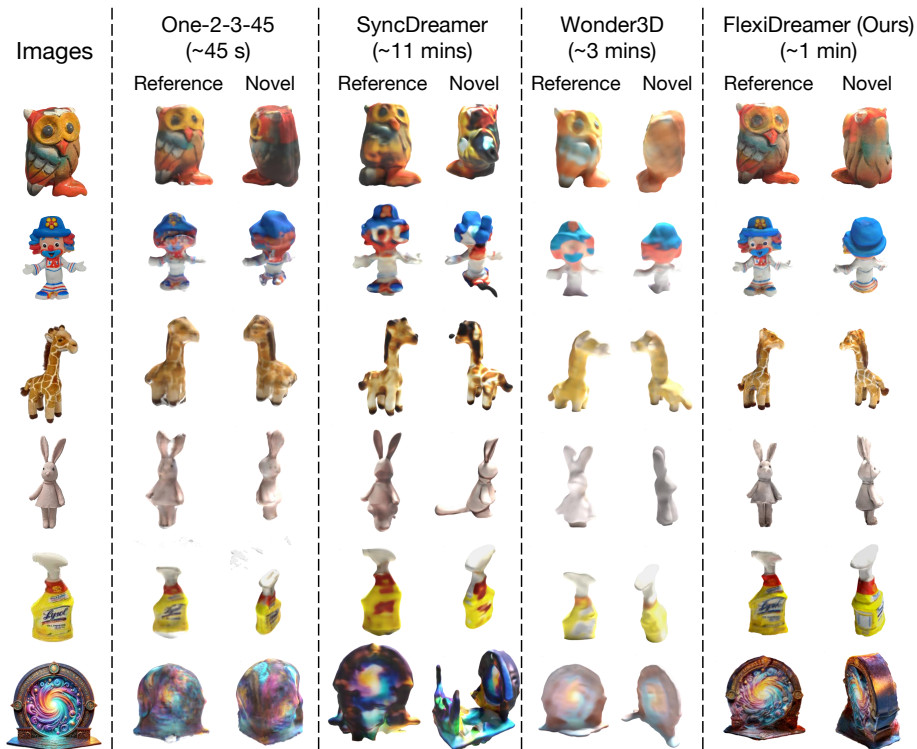


Fig. 4: The qualitative comparisons with baselines in terms of the generated textured meshes. It reveals a superior performance of FlexiDreamer in reconstructing both geometry and texture details from single-view images.

Figure 4 visualizes some examples of the shapes generated from single images in geometry, texture and speed. Specifically, One-2-3-45 generates meshes from inconsistent multi-view results of Zero-1-to-3 [34], thus suffering from distortion. The 3D shapes reconstructed by SyncDreamer lack surface details and exhibit poor-quality texture. Meshes produced by Wonder3D fail to recover the abundant information that the input images provide. Moreover, the baselines also implement Marching Cubes [39] on trained SparseNeuS [38] or NeuS [70] for 3D content extraction, leading to surface artifacts such as unevenness in their meshes.

In comparison, we observe that FlexiDreamer produces sharper geometric details, more distinct textures, and more consistent surfaces in a short amount of time. This outstanding performance benefits not only from the effective integration of a multi-resolution hashgrid encoding scheme when learning geometry and texture, but also from the usage of FlexiCubes [57] to bypass post-processing of NeRF representations.

Table 1: Quantitative results compared with baseline methods in Chamfer Distance and Volume IoU metric. The ground truth is prepared by the Google Scanned Object (GSO) [14] dataset.

Method	Chamfer Dist↓	Volume IoU↑
Wonder3D [37]	0.0186	0.4398
SyncDreamer [35]	0.0140	0.3900
One-2-3-45 [33]	0.0172	0.4463
Magic123 [50]	0.0188	0.3714
Ours	0.0112	0.4332

Table 2: Quantitative results compared with baseline methods in SSIM and LPIPS metric. The ground truth is prepared by predefined-view images rendered from GSO dataset.

Method	SSIM↑	LPIPS↓
Wonder3D [37]	0.8121	0.2554
SyncDreamer [35]	0.8165	0.2591
One-2-3-45 [33]	0.8084	0.2625
Magic123 [50]	0.7984	0.2442
Ours	0.8405	0.2308

5.2 Quantitative Results

We choose Wonder3D, SyncDreamer, One-2-3-45 and Magic123 as our baselines to conduct quantitative comparison in the single image-to-3D task. The inputs are RGB images rendered from the Google Scanned Object (GSO) dataset [14] in a selected view. Before evaluation, the generated and ground-truth shapes are initially scaled to an identical size, with their centers aligned at the same position. Subsequently, we employ two widely used metrics, namely Chamfer Distances (CD) and Volume Intersection over Union (Volume IoU), to assess the similarity in reconstructed geometry between them. Table 1 demonstrates that our method outperforms other methods and reconstructs the most accurate geometric shapes. Additionally, to evaluate texture quality, we render 24 images from ground-truth and generated meshes respectively. Then we use SSIM [77] and LPIPS [89] to evaluate the similarity of the texture. Table 2 summarizes that our method outperforms all the baselines, which means it has the ability to recover realistic texture.

5.3 Abalation Study

Smooth Regularization To assess the effectiveness of the two smooth regularizations we employed, which are laplacian regularization and normal consistency regularization, we conduct experiments in generating a mushroom featuring a smooth cap. The visualization results are depicted in Figure 5. It is noticed that

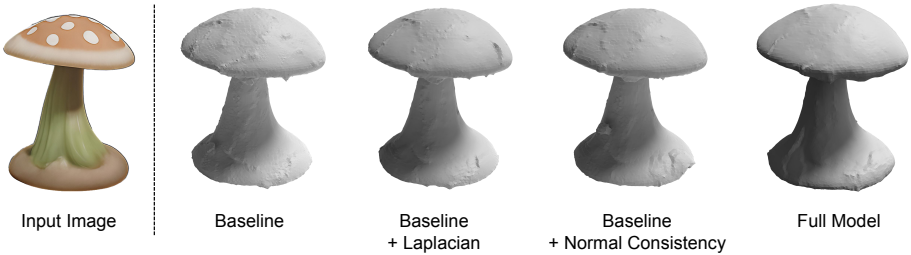


Fig. 5: Ablation study on the strategies for smoothing mesh surface: laplacian regularization and normal consistency regularization. The laplacian smoothing term can smooth the surface of the mesh at a global scale while normal consistency constraint helps reduce high-frequency noises.

the baseline model’s surface exhibits severe unevenness and protrusions. Incorporating either laplacian smoothness or normal consistency constraints can help mitigate the noisy surfaces. Specifically, the laplacian penalty term is adept at smoothing the mesh surface at a global scale. Meanwhile, the normal consistency term plays a pivotal role in diminishing high-frequency noises, thereby enhancing the overall quality of the mesh structure. Finally, the combination of both smoothing strategies yields optimal performance, resulting in clean surfaces while retaining intricate details.

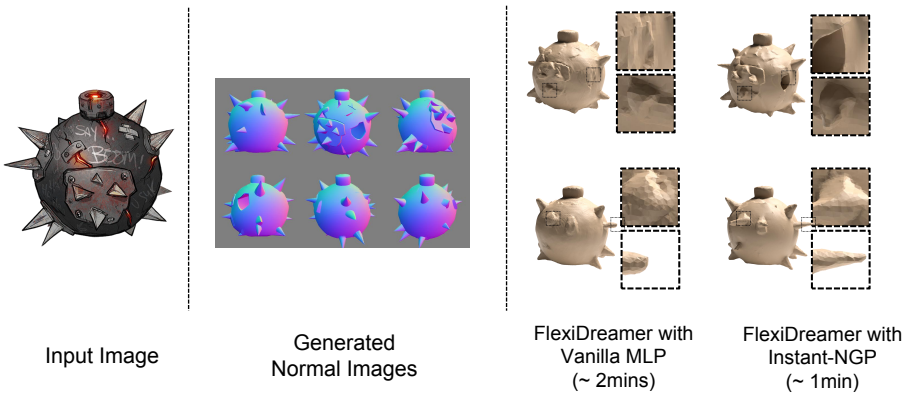


Fig. 6: Ablation study on FlexiDreamer employed by different neural network structures in geometric shape and generation speed. Taking the normal maps generated from Zero123++ as inference, the signed distance neural network implemented by vanilla MLP reconstructs a smoother surface than Instant-NGP and also suffers from a longer generation time.

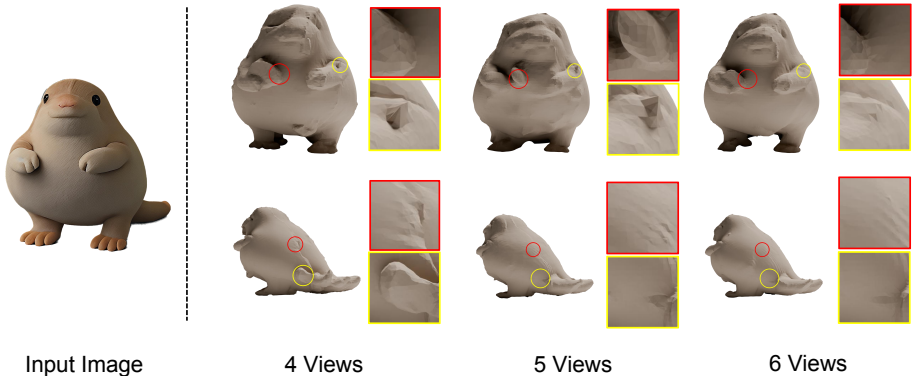


Fig. 7: Ablation study on different numbers of input views. With an increasing number of supervised viewpoints, the accuracy of the reconstructed mesh improves.

Neural Network Structure To evaluate the feasibility of adopting an Instant-NGP [45] network for implementing neural fields, especially for the signed distance neural field, we conduct a comparison with its counterpart, where the signed distance network is replaced by a vanilla MLP while keeping other components unchanged, in terms of mesh surface and generation speed. The vanilla MLP network is implemented by 6 layers of multi-layer perceptions with 64 hidden dims to successfully obtain the target mesh, while Instant-NGP only requires one layer to achieve a high-quality geometry. As illustrated in Figure 6, the mesh surface generated by the vanilla MLP network appears overly smooth and fails to capture the sharp features present in the generated normal maps. Furthermore, since vanilla MLP requires more layers than Instant-NGP to learn a good shape, it takes a longer time to converge, resulting in a slower generation speed. Therefore, Instant-NGP is more suitable for our signed distance neural field.

The number of input views Figure 7 showcases the impact of varying the number of input images derived from the multi-view diffusion model in Zero123++ [58]. The 4-view and 5-view settings constitute partial components of the input images within the 6-view setting. We select two viewpoints from the generated meshes to compare the surface geometry across three settings. It is observed that in comparison to the 6-view setting, the meshes obtained under the 4-view and 5-view configurations exhibit noticeable imperfections. These imperfections, characterized by unevenness or additional protrusions, are particularly obvious in the circled regions. Moreover, the extent of these imperfections is more pronounced in the case of the 4-view setting. This finding indicates that fewer views are insufficient to adequately capture the total information of the target object, and supervision with fewer views worsens occlusion issues and diminishes generation quality.

6 Conclusion

In this paper, we introduce FlexiDreamer, a novel approach targeted at rapidly generating high-quality textured meshes from single-view images. By leveraging FlexiCubes, FlexiDreamer realizes an end-to-end acquisition of target assets without the need for negative post-processing operations, meanwhile avoiding the slow convergence issue in NeRF-based representations in previous studies. We enhance the original encoding pattern of FlexiCubes in the signed distance field by adopting a multi-resolution hashgrid encoding scheme. This scheme progressively activates the encoding levels, facilitating the capture of geometric details for per-step optimization. Moreover, we integrate a texture neural field to provide texture for the mesh. Experimental results demonstrate that our method delivers comprehensive geometry and realistic texture compared to other current state-of-the-art single image-to-3D frameworks.

7 Potential Negative Impact

Our method excels in producing hyper-realistic 3D assets within a short amount of time, thanks to its crafted generation technologies. However, the high fidelity of generated results might raise a concern about misuse by malicious entities. These individuals could exploit this technology to create deepfakes or counterfeit products, posing significant risks to various aspects of society. Such misuse could lead to severe consequences, including damaging individuals' reputations, spreading misinformation, and eroding trust in digital media platforms. Therefore, it is necessary for both developers and users to remain vigilant to prevent the occurrence of such harmful practices.



Fig. 8: Some failure cases. The mesh in the first row has more than four legs due to the limited views of supervision. The mesh in the second row suffers from a multi-face problem because of the inconsistency existing in the images generated from the diffusion model.

8 Limitations

While FlexiDreamer demonstrates promising performance in generating 3D objects from single inputs, it still has limitations that the current framework cannot fully address. Given that our model is essentially a multi-view reconstruction model, the quality of 3D assets is heavily dependent on the quality of generated images. However, existing multi-view diffusion models in [37, 51, 58] are still imperfect. There still exists 3D inconsistency among multi-view images, which will potentially mislead the reconstruction model to produce floaters or mismatches. Additionally, the limited perspectives of images also hinder our framework to accurately construct objects. Figure 8 shows some failure cases.

References

1. Atzmon, M., Lipman, Y.: Sal: Sign agnostic learning of shapes from raw data. In: Proceedings of the IEEE/CVF Conference on Computer Vision and Pattern Recognition. pp. 2565–2574 (2020) 9
2. Cao, Z., Hong, F., Wu, T., Pan, L., Liu, Z.: Large-vocabulary 3d diffusion model with transformer (2023) 4
3. Chan, E.R., Lin, C.Z., Chan, M.A., Nagano, K., Pan, B., Mello, S.D., Gallo, O., Guibas, L., Tremblay, J., Khamis, S., Karras, T., Wetzstein, G.: Efficient geometry-aware 3d generative adversarial networks (2022) 3
4. Chen, A., Xu, Z., Geiger, A., Yu, J., Su, H.: Tensorf: Tensorial radiance fields. In: European Conference on Computer Vision. pp. 333–350. Springer (2022) 4
5. Chen, H., Gu, J., Chen, A., Tian, W., Tu, Z., Liu, L., Su, H.: Single-stage diffusion nerf: A unified approach to 3d generation and reconstruction (2023) 4
6. Chen, R., Chen, Y., Jiao, N., Jia, K.: Fantasia3d: Disentangling geometry and appearance for high-quality text-to-3d content creation. arXiv preprint arXiv:2303.13873 (2023) 2, 4
7. Chen, Y., Chen, Z., Zhang, C., Wang, F., Yang, X., Wang, Y., Cai, Z., Yang, L., Liu, H., Lin, G.: Gaussianeditor: Swift and controllable 3d editing with gaussian splatting (2023) 4
8. Chen, Y., Zhang, C., Yang, X., Cai, Z., Yu, G., Yang, L., Lin, G.: It3d: Improved text-to-3d generation with explicit view synthesis (2023) 4
9. Chen, Z., Wang, F., Liu, H.: Text-to-3d using gaussian splatting. arXiv preprint arXiv:2309.16585 (2023) 4
10. Chou, G., Bahat, Y., Heide, F.: Diffusion-sdf: Conditional generative modeling of signed distance functions (2023) 4
11. Deitke, M., Liu, R., Wallingford, M., Ngo, H., Michel, O., Kusupati, A., Fan, A., Laforte, C., Voleti, V., Gadre, S.Y., et al.: Objaverse-xl: A universe of 10m+ 3d objects. Advances in Neural Information Processing Systems 36 (2024) 9
12. Deitke, M., Schwenk, D., Salvador, J., Weihs, L., Michel, O., Vanderbilt, E., Schmidt, L., Ehsani, K., Kembhavi, A., Farhadi, A.: Objaverse: A universe of annotated 3d objects. In: Proceedings of the IEEE/CVF Conference on Computer Vision and Pattern Recognition. pp. 13142–13153 (2023) 9
13. Ding, L., Dong, S., Huang, Z., Wang, Z., Zhang, Y., Gong, K., Xu, D., Xue, T.: Text-to-3d generation with bidirectional diffusion using both 2d and 3d priors (2023) 4

14. Downs, L., Francis, A., Koenig, N., Kinman, B., Hickman, R., Reymann, K., McHugh, T.B., Vanhoucke, V.: Google scanned objects: A high-quality dataset of 3d scanned household items (2022) [11](#)
15. Fridovich-Keil, S., Meanti, G., Warburg, F., Recht, B., Kanazawa, A.: K-planes: Explicit radiance fields in space, time, and appearance (2023) [4](#)
16. Gao, J., Shen, T., Wang, Z., Chen, W., Yin, K., Li, D., Litany, O., Gojcic, Z., Fidler, S.: Get3d: A generative model of high quality 3d textured shapes learned from images. *Advances In Neural Information Processing Systems* **35**, 31841–31854 (2022) [4](#)
17. Gropp, A., Yariv, L., Haim, N., Atzmon, M., Lipman, Y.: Implicit geometric regularization for learning shapes. *arXiv preprint arXiv:2002.10099* (2020) [9](#)
18. Gupta, A., Xiong, W., Nie, Y., Jones, I., Oğuz, B.: 3dgen: Triplane latent diffusion for textured mesh generation (2023) [4](#)
19. Hong, Y., Zhang, K., Gu, J., Bi, S., Zhou, Y., Liu, D., Liu, F., Sunkavalli, K., Bui, T., Tan, H.: Lrm: Large reconstruction model for single image to 3d (2023) [3](#), [4](#)
20. Ju, T., Losasso, F., Schaefer, S., Warren, J.: Dual contouring of hermite data. In: *Proceedings of the 29th annual conference on Computer graphics and interactive techniques*. pp. 339–346 (2002) [5](#)
21. Jun, H., Nichol, A.: Shap-e: Generating conditional 3d implicit functions. *arXiv preprint arXiv:2305.02463* (2023) [4](#)
22. Kerbl, B., Kopanas, G., Leimkühler, T., Drettakis, G.: 3d gaussian splatting for real-time radiance field rendering (2023) [4](#)
23. Kingma, D.P., Ba, J.: Adam: A method for stochastic optimization. *arXiv preprint arXiv:1412.6980* (2014) [9](#)
24. Laine, S., Hellsten, J., Karras, T., Seol, Y., Lehtinen, J., Aila, T.: Modular primitives for high-performance differentiable rendering. *ACM Transactions on Graphics* **39**(6) (2020) [8](#)
25. Li, J., Tan, H., Zhang, K., Xu, Z., Luan, F., Xu, Y., Hong, Y., Sunkavalli, K., Shakhnarovich, G., Bi, S.: Instant3d: Fast text-to-3d with sparse-view generation and large reconstruction model (2023) [3](#), [4](#), [5](#)
26. Li, W., Chen, R., Chen, X., Tan, P.: Sweetdreamer: Aligning geometric priors in 2d diffusion for consistent text-to-3d (2023) [4](#), [6](#)
27. Li, Z., Müller, T., Evans, A., Taylor, R.H., Unberath, M., Liu, M.Y., Lin, C.H.: Neuralangelo: High-fidelity neural surface reconstruction. In: *IEEE Conference on Computer Vision and Pattern Recognition (CVPR)* (2023) [6](#), [21](#)
28. Liang, Y., Yang, X., Lin, J., Li, H., Xu, X., Chen, Y.: Luciddreamer: Towards high-fidelity text-to-3d generation via interval score matching (2023) [4](#)
29. Lin, C.H., Gao, J., Tang, L., Takikawa, T., Zeng, X., Huang, X., Kreis, K., Fidler, S., Liu, M.Y., Lin, T.Y.: Magic3d: High-resolution text-to-3d content creation. In: *IEEE Conference on Computer Vision and Pattern Recognition (CVPR)* (2023) [2](#), [4](#)
30. Lin, Y., Han, H., Gong, C., Xu, Z., Zhang, Y., Li, X.: Consistent123: One image to highly consistent 3d asset using case-aware diffusion priors (2024) [4](#)
31. Ling, H., Kim, S.W., Torralba, A., Fidler, S., Kreis, K.: Align your gaussians: Text-to-4d with dynamic 3d gaussians and composed diffusion models (2024) [4](#)
32. Liu, M., Shi, R., Chen, L., Zhang, Z., Xu, C., Wei, X., Chen, H., Zeng, C., Gu, J., Su, H.: One-2-3-45++: Fast single image to 3d objects with consistent multi-view generation and 3d diffusion. *arXiv preprint arXiv:2311.07885* (2023) [6](#)
33. Liu, M., Xu, C., Jin, H., Chen, L., Xu, Z., Su, H., et al.: One-2-3-45: Any single image to 3d mesh in 45 seconds without per-shape optimization. *arXiv preprint arXiv:2306.16928* (2023) [3](#), [4](#), [5](#), [9](#), [11](#), [21](#), [23](#)

34. Liu, R., Wu, R., Van Hoorick, B., Tokmakov, P., Zakharov, S., Vondrick, C.: Zero-1-to-3: Zero-shot one image to 3d object. In: Proceedings of the IEEE/CVF International Conference on Computer Vision. pp. 9298–9309 (2023) [4](#), [6](#), [10](#)
35. Liu, Y., Lin, C., Zeng, Z., Long, X., Liu, L., Komura, T., Wang, W.: Syncdreamer: Generating multiview-consistent images from a single-view image. arXiv preprint arXiv:2309.03453 (2023) [3](#), [4](#), [5](#), [6](#), [9](#), [11](#), [23](#)
36. Liu, Z., Feng, Y., Black, M.J., Nowrouzezahrai, D., Paull, L., Liu, W.: Meshdiffusion: Score-based generative 3d mesh modeling (2023) [4](#)
37. Long, X., Guo, Y.C., Lin, C., Liu, Y., Dou, Z., Liu, L., Ma, Y., Zhang, S.H., Habermann, M., Theobalt, C., et al.: Wonder3d: Single image to 3d using cross-domain diffusion. arXiv preprint arXiv:2310.15008 (2023) [3](#), [4](#), [5](#), [9](#), [11](#), [15](#), [23](#)
38. Long, X., Lin, C., Wang, P., Komura, T., Wang, W.: Sparseneus: Fast generalizable neural surface reconstruction from sparse views (2022) [3](#), [4](#), [10](#)
39. Lorensen, W.E., Cline, H.E.: Marching cubes: A high resolution 3d surface construction algorithm. In: Proceedings of the 14th Annual Conference on Computer Graphics and Interactive Techniques. p. 163–169. SIGGRAPH '87, Association for Computing Machinery, New York, NY, USA (1987). <https://doi.org/10.1145/37401.37422>, <https://doi.org/10.1145/37401.37422> [3](#), [4](#), [5](#), [10](#)
40. Lorraine, J., Xie, K., Zeng, X., Lin, C.H., Takikawa, T., Sharp, N., Lin, T.Y., Liu, M.Y., Fidler, S., Lucas, J.: Att3d: Amortized text-to-3d object synthesis (2023) [4](#)
41. Luan, F., Zhao, S., Bala, K., Dong, Z.: Unified shape and svbrdf recovery using differentiable monte carlo rendering (2021) [9](#)
42. Melas-Kyriazi, L., Rupprecht, C., Laina, I., Vedaldi, A.: Realfusion: 360deg reconstruction of any object from a single image (2023) [4](#)
43. Mercier, A., Nakhli, R., Reddy, M., Yasarla, R., Cai, H., Porikli, F., Berger, G.: Hexagen3d: Stablediffusion is just one step away from fast and diverse text-to-3d generation. arXiv preprint arXiv:2401.07727 (2024) [4](#)
44. Mildenhall, B., Srinivasan, P.P., Tancik, M., Barron, J.T., Ramamoorthi, R., Ng, R.: Nerf: Representing scenes as neural radiance fields for view synthesis (2020) [3](#)
45. Müller, T., Evans, A., Schied, C., Keller, A.: Instant neural graphics primitives with a multiresolution hash encoding. ACM Trans. Graph. **41**(4), 102:1–102:15 (Jul 2022). <https://doi.org/10.1145/3528223.3530127>, <https://doi.org/10.1145/3528223.3530127> [3](#), [6](#), [13](#)
46. Müller, N., Siddiqui, Y., Porzi, L., Bulò, S.R., Kontschieder, P., Nießner, M.: Diffrf: Rendering-guided 3d radiance field diffusion (2023) [4](#)
47. Nichol, A., Jun, H., Dhariwal, P., Mishkin, P., Chen, M.: Point-e: A system for generating 3d point clouds from complex prompts (2022) [4](#)
48. Nielson, G.M.: Dual marching cubes. In: IEEE visualization 2004. pp. 489–496. IEEE (2004) [5](#), [8](#)
49. Poole, B., Jain, A., Barron, J.T., Mildenhall, B.: Dreamfusion: Text-to-3d using 2d diffusion. arXiv (2022) [2](#), [4](#)
50. Qian, G., Mai, J., Hamdi, A., Ren, J., Siarohin, A., Li, B., Lee, H.Y., Skorokhodov, I., Wonka, P., Tulyakov, S., Ghanem, B.: Magic123: One image to high-quality 3d object generation using both 2d and 3d diffusion priors (2023) [11](#)
51. Qiu, L., Chen, G., Gu, X., Zuo, Q., Xu, M., Wu, Y., Yuan, W., Dong, Z., Bo, L., Han, X.: Richdreamer: A generalizable normal-depth diffusion model for detail richness in text-to-3d. arXiv preprint arXiv:2311.16918 (2023) [4](#), [15](#)
52. Raj, A., Kaza, S., Poole, B., Niemeyer, M., Ruiz, N., Mildenhall, B., Zada, S., Aberman, K., Rubinstein, M., Barron, J., Li, Y., Jampani, V.: Dreambooth3d: Subject-driven text-to-3d generation (2023) [4](#)

53. Ren, J., Pan, L., Tang, J., Zhang, C., Cao, A., Zeng, G., Liu, Z.: Dreamgaussian4d: Generative 4d gaussian splatting (2023) [4](#)
54. Rombach, R., Blattmann, A., Lorenz, D., Esser, P., Ommer, B.: High-resolution image synthesis with latent diffusion models. In: Proceedings of the IEEE/CVF conference on computer vision and pattern recognition. pp. 10684–10695 (2022) [2](#), [4](#)
55. Seo, J., Jang, W., Kwak, M.S., Kim, H., Ko, J., Kim, J., Kim, J.H., Lee, J., Kim, S.: Let 2d diffusion model know 3d-consistency for robust text-to-3d generation (2024) [4](#)
56. Shen, T., Gao, J., Yin, K., Liu, M.Y., Fidler, S.: Deep marching tetrahedra: a hybrid representation for high-resolution 3d shape synthesis (2021) [5](#)
57. Shen, T., Munkberg, J., Hasselgren, J., Yin, K., Wang, Z., Chen, W., Gojcic, Z., Fidler, S., Sharp, N., Gao, J.: Flexible isosurface extraction for gradient-based mesh optimization. *ACM Trans. Graph.* **42**(4) (jul 2023). <https://doi.org/10.1145/3592430>, <https://doi.org/10.1145/3592430> [3](#), [4](#), [5](#), [7](#), [10](#), [21](#)
58. Shi, R., Chen, H., Zhang, Z., Liu, M., Xu, C., Wei, X., Chen, L., Zeng, C., Su, H.: Zero123++: a single image to consistent multi-view diffusion base model (2023) [4](#), [6](#), [13](#), [15](#), [21](#)
59. Shi, R., Wei, X., Wang, C., Su, H.: Zerorf: Fast sparse view 360deg reconstruction with zero pretraining (2023) [4](#)
60. Shi, Y., Wang, P., Ye, J., Long, M., Li, K., Yang, X.: Mvdream: Multi-view diffusion for 3d generation (2023) [2](#), [4](#), [6](#)
61. Shi, Y., Wang, J., Cao, H., Tang, B., Qi, X., Yang, T., Huang, Y., Liu, S., Zhang, L., Shum, H.Y.: Toss:high-quality text-guided novel view synthesis from a single image (2023) [4](#)
62. Sun, J., Zhang, B., Shao, R., Wang, L., Liu, W., Xie, Z., Liu, Y.: Dreamcraft3d: Hierarchical 3d generation with bootstrapped diffusion prior (2023) [4](#)
63. Szymanowicz, S., Rupprecht, C., Vedaldi, A.: Splatter image: Ultra-fast single-view 3d reconstruction (2023) [4](#)
64. Takikawa, T., Litalien, J., Yin, K., Kreis, K., Loop, C., Nowrouzezahrai, D., Jacobson, A., McGuire, M., Fidler, S.: Neural geometric level of detail: Real-time rendering with implicit 3d shapes (2021) [6](#)
65. Tang, J., Chen, Z., Chen, X., Wang, T., Zeng, G., Liu, Z.: Lgm: Large multi-view gaussian model for high-resolution 3d content creation. *arXiv preprint arXiv:2402.05054* (2024) [4](#)
66. Tang, J., Ren, J., Zhou, H., Liu, Z., Zeng, G.: Dreamgaussian: Generative gaussian splatting for efficient 3d content creation (2023) [4](#), [21](#)
67. Tang, J., Wang, T., Zhang, B., Zhang, T., Yi, R., Ma, L., Chen, D.: Make-it-3d: High-fidelity 3d creation from a single image with diffusion prior (2023) [4](#)
68. Tochilkin, D., Pankratz, D., Liu, Z., Huang, Z., Letts, A., Li, Y., Liang, D., Laforte, C., Jampani, V., Cao, Y.P.: Tripotr: Fast 3d object reconstruction from a single image (2024) [4](#)
69. Wang, H., Du, X., Li, J., Yeh, R.A., Shakhnarovich, G.: Score jacobian chaining: Lifting pretrained 2d diffusion models for 3d generation (2022) [4](#)
70. Wang, P., Liu, L., Liu, Y., Theobalt, C., Komura, T., Wang, W.: Neus: Learning neural implicit surfaces by volume rendering for multi-view reconstruction (2023) [3](#), [4](#), [10](#)
71. Wang, P., Shi, Y.: Imagedream: Image-prompt multi-view diffusion for 3d generation (2023) [2](#), [4](#), [6](#)

72. Wang, P., Tan, H., Bi, S., Xu, Y., Luan, F., Sunkavalli, K., Wang, W., Xu, Z., Zhang, K.: Pf-lrm: Pose-free large reconstruction model for joint pose and shape prediction (2023) [4](#)
73. Wang, T., Zhang, B., Zhang, T., Gu, S., Bao, J., Baltrusaitis, T., Shen, J., Chen, D., Wen, F., Chen, Q., Guo, B.: Rodin: A generative model for sculpting 3d digital avatars using diffusion (2022) [4](#)
74. Wang, X., Wang, Y., Ye, J., Wang, Z., Sun, F., Liu, P., Wang, L., Sun, K., Wang, X., He, B.: Animatabledreamer: Text-guided non-rigid 3d model generation and reconstruction with canonical score distillation. arXiv preprint arXiv:2312.03795 (2023) [4](#)
75. Wang, Z., Lu, C., Wang, Y., Bao, F., Li, C., Su, H., Zhu, J.: Prolificdreamer: High-fidelity and diverse text-to-3d generation with variational score distillation. In: Advances in Neural Information Processing Systems (NeurIPS) (2023) [2](#), [4](#)
76. Wang, Z., Wang, Y., Chen, Y., Xiang, C., Chen, S., Yu, D., Li, C., Su, H., Zhu, J.: Crm: Single image to 3d textured mesh with convolutional reconstruction model. arXiv preprint arXiv:2403.05034 (2024) [4](#)
77. Wang, Z., Bovik, A.C., Sheikh, H.R., Simoncelli, E.P.: Image quality assessment: from error visibility to structural similarity. IEEE transactions on image processing **13**(4), 600–612 (2004) [11](#)
78. Xu, D., Yuan, Y., Mardani, M., Liu, S., Song, J., Wang, Z., Vahdat, A.: Agg: Amortized generative 3d gaussians for single image to 3d (2024) [4](#)
79. Xu, Y., Shi, Z., Yifan, W., Chen, H., Yang, C., Peng, S., Shen, Y., Wetzstein, G.: Grm: Large gaussian reconstruction model for efficient 3d reconstruction and generation (2024) [4](#)
80. Xu, Y., Tan, H., Luan, F., Bi, S., Wang, P., Li, J., Shi, Z., Sunkavalli, K., Wetzstein, G., Xu, Z., Zhang, K.: Dmv3d: Denoising multi-view diffusion using 3d large reconstruction model (2023) [4](#)
81. Yang, J., Cheng, Z., Duan, Y., Ji, P., Li, H.: Consistnet: Enforcing 3d consistency for multi-view images diffusion (2023) [4](#)
82. Yariv, L., Puny, O., Neverova, N., Gafni, O., Lipman, Y.: Mosaic-sdf for 3d generative models (2023) [4](#)
83. Ye, J., Wang, P., Li, K., Shi, Y., Wang, H.: Consistent-1-to-3: Consistent image to 3d view synthesis via geometry-aware diffusion models (2023) [4](#)
84. Ye, J., Liu, F., Li, Q., Wang, Z., Wang, Y., Wang, X., Duan, Y., Zhu, J.: Dreamreward: Text-to-3d generation with human preference (2024) [4](#)
85. Yi, T., Fang, J., Wang, J., Wu, G., Xie, L., Zhang, X., Liu, W., Tian, Q., Wang, X.: Gaussiandreamer: Fast generation from text to 3d gaussians by bridging 2d and 3d diffusion models (2023) [4](#)
86. Yin, Y., Xu, D., Wang, Z., Zhao, Y., Wei, Y.: 4dgen: Grounded 4d content generation with spatial-temporal consistency (2024) [4](#)
87. Zhang, J., Tang, Z., Pang, Y., Cheng, X., Jin, P., Wei, Y., Ning, M., Yuan, L.: Repaint123: Fast and high-quality one image to 3d generation with progressive controllable 2d repainting (2023) [4](#)
88. Zhang, L., Rao, A., Agrawala, M.: Adding conditional control to text-to-image diffusion models (2023) [6](#)
89. Zhang, R., Isola, P., Efros, A.A., Shechtman, E., Wang, O.: The unreasonable effectiveness of deep features as a perceptual metric. In: Proceedings of the IEEE conference on computer vision and pattern recognition. pp. 586–595 (2018) [11](#)
90. Zhao, Z., Liu, W., Chen, X., Zeng, X., Wang, R., Cheng, P., Fu, B., Chen, T., Yu, G., Gao, S.: Michelangelo: Conditional 3d shape generation based on shape-image-text aligned latent representation (2023) [4](#)

91. Zou, Z.X., Yu, Z., Guo, Y.C., Li, Y., Liang, D., Cao, Y.P., Zhang, S.H.: Triplane meets gaussian splatting: Fast and generalizable single-view 3d reconstruction with transformers (2023) [4](#)

Appendix

A More Implementation Details

In our experimental setup, we adhere to a uniform set of hyperparameters across all experiments. Optimization of parameters in both the signed distance neural network and the texture neural network is conducted utilizing Adam optimizer with a learning rate of 1e-3 and 1e-2 respectively for 600 training iterations. Within the positional encoding scheme employed in both networks, the resolution of hierarchical hash grids is chosen to be a geometric progression between the coarsest and finest resolutions $[2^4, 2^{10}]$ every 100 iterations, and each hash entry has a channel of 2. The geometry constraints weights, denoted as λ_{normal} and λ_{mask} , are meticulously configured to 30.0 and 500.0 respectively for geometry supervision, while λ_{rgb} is carefully set to 1.0 to supervise a more realistic texture.

When computing the gradients of signed distance values in the eikonal loss equation 5, numerical gradients, as advocated by [27], are preferred due to their continuity across 3D space in trilinear interpolation rather than analytic gradients. To compute the signed distance value’s numerical gradient at a selected point $\mathbf{x}_i = (x_i, y_i, z_i)$, additional sampled points along each axis within a distance ϵ are needed. For instance, the x -component of signed distance value’s gradient at \mathbf{x}_i can be found as:

$$\nabla_x g(\mathbf{x}_i) = \frac{g(e(\mathbf{x}_i + \boldsymbol{\epsilon}_x)) - g(e(\mathbf{x}_i - \boldsymbol{\epsilon}_x))}{2\epsilon} \quad (6)$$

where $\boldsymbol{\epsilon}_x = [\epsilon, 0, 0]$. g refers to the signed distance function while e stands for the hashgrid positional encoding scheme. The distance ϵ between two neighbour points is initialized by the coarsest hash grid size and exponentially diminishes to accommodate different hash grid sizes in coarse-to-fine positional encoding. The weighting factor assigned to the eikonal loss, denoted as $\lambda_{eikonal}$, is set to 0.1.

For multi-view image generation, we adopt Zero123++ (v1.2) [58] as our multi-view diffusion model. The guidance of Zero123++ is configured to 4 while the number of inference steps is set to 75. The multi-view generated images are cropped into a resolution of 256×256 for subsequent few-shot reconstruction in FlexiDreamer. Additionally, we incorporate laplacian regularization and normal consistency regularization into our framework to obtain a more smooth mesh surface, carefully setting $\lambda_{laplacian}$ to 50.0 and $\lambda_{consistency}$ to 3.0. Our implementation is built on Zero123++ and FlexiCubes [57]. The training process of FlexiDreamer takes roughly 1 minute on an 80G A100 NVIDIA GPU.

B Camera Settings

We inherit the camera settings from Zero123++: In order to circumvent the error in the elevation estimation module incorporated in previous pipelines, such as One-2-3-45 [33] and DreamGaussian [66], we use camera poses with relative

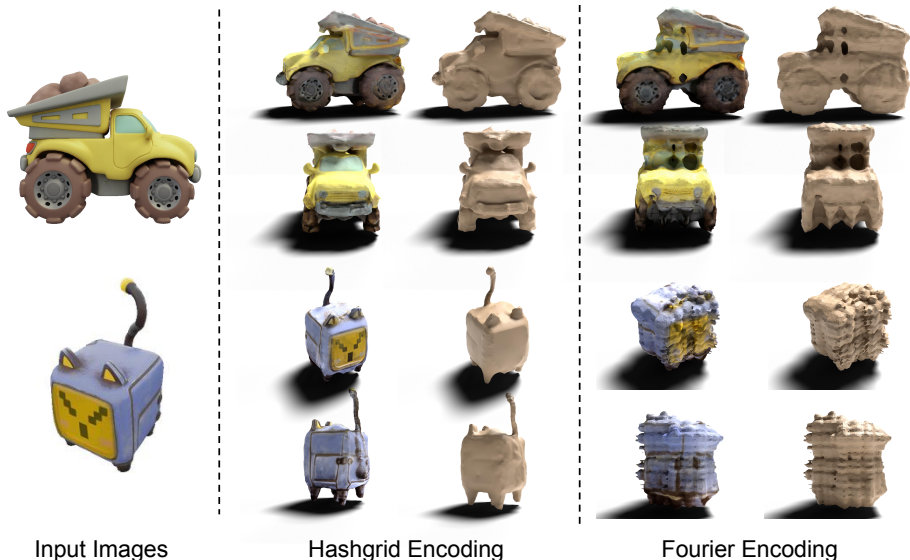


Fig. 9: The visualization of different positional encoding pattern’s performance. The hashgrid encoding scheme demonstrates superior capability in capturing finer geometric details compared to the Fourier encoding method.

azimuth and absolute elevation angles to the input view for novel view synthesis to minimize the orientation inconsistency. To be more specific, the six poses comprise interleaving elevations of -10° and 20° , accompanied by azimuths that span from 30° to 330° with an increase by 60° for each pose. These carefully chosen camera poses can totally scan the whole object. Moreover, we adopt a perspective camera system and the camera is positioned at a distance of 3.0 meters from the coordinate origin, i.e. the radial distance is 3.0.

C Additional Ablation Studies

Encodings An appropriate selection of position encoding patterns in our signed distance neural network is pivotal for our reconstruction framework to capture finer local details. Since both multi-resolution hashgrid and Fourier encoding are capable of accommodating high-dimensional positional features, we evaluate them on the position-dependent component of our signed distance neural network using the same encoding level. As depicted in Figure 9, Fourier encoding does not guarantee a sharper geometry in spite of an acceptable rendering. The geometric details of mesh in Fourier are less than hashgrid. A plausible explanation for this observation is that Fourier encoding, based on the Fourier transform, only works efficiently for examples with periodic or repetitive structures. In contrast, hashgrid encoding outperforms in capturing local spatial structures for arbitrary samples by assigning a unique encode to each hierarchical grid cell.

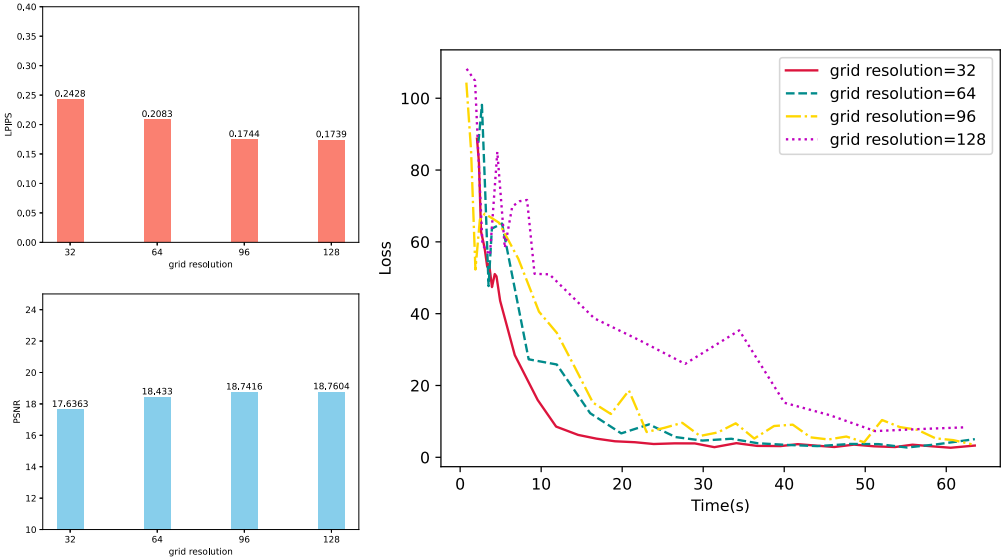


Fig. 10: Convergence curves of the model with different training grid resolutions. PSNR and LPIPS metrics of the generated meshes surface are also compared.

Training grid resolution The resolution of the 3D coordinates volume depicted in Figure 2 determines the computational complexity and surface details of the iteratively extracted mesh. In order to choose a suitable resolution, we conduct experiments using various resolutions, namely 32, 64, 96, and 128. As illustrated in Figure 10, we plot curves of loss under different settings throughout the training process. We also evaluate both PSNR and LPIPS metrics of the rendered normal images derived from the final extraction mesh. We notice that although the ultimately generated mesh enhances performance with increasing resolution, the model exhibits a slower convergence. Moreover, the convergence time at the resolution of 128 is significantly longer than the other three scenarios. However, compared with resolution 96, where the model already exhibits an acceptable performance, the improvements achieved at resolution 128 are marginal. As a result, a grid resolution of 96 is selected to strike a balance between generation speed and quality.

D More Comparisons

We additionally compare FlexiDreamer with recent methods Wonder3D [37], SyncDreamer [35] and One-2-3-45 [33] in Figure 11. FlexiDreamer outperforms all the baselines significantly in terms of 3D geometry, texture quality and generation speed.



Fig. 11: Qualitative comparisons: We compare FlexiDreamer with recent state-of-art single image-to-3D approaches.